



Cite this: *Phys. Chem. Chem. Phys.*,  
2021, **23**, 22661

# Early stages of aggregation in fluid mixtures of dimers and spheres: a theoretical and simulation study

Gianmarco Munaò, \* Santi Prestipino and Dino Costa

We use Monte Carlo simulation and the Reference Interaction Site Model (RISM) theory of molecular fluids to investigate a simple model of colloidal mixture consisting of dimers, made up of two tangent hard monomers of different size, and hard spheres. In addition to steric repulsion, the two species interact *via* a square-well attraction only between small monomers and spheres. Recently, we have characterized the low-temperature regime of this mixture by Monte Carlo, reporting on the spontaneous formation of a wide spectrum of supramolecular aggregates [Prestipino *et al.*, *J. Phys. Chem. B*, 2019, **123**, 9272]. Here we focus on a regime of temperatures where, on cooling, the appearance of local inhomogeneities first, and the early stages of aggregation thereafter, are observed. In particular, we find signatures of aggregation in the onset of a low-wavevector peak in the structure factors of the mixture, as computed by both theory and simulation. Then, we link the structural information to the microscopic arrangement through a detailed cluster analysis of Monte Carlo configurations. In this regard, we devise a novel method to compute the maximum distance for which two spheres can be regarded as bonded together, a crucial issue in the proper identification of fluid aggregates. The RISM theory provides relatively accurate structural and thermodynamic predictions in comparison with Monte Carlo, but with slightly degrading performances as the fluid progresses inside the locally inhomogeneous phase. Our study certifies the efficacy of the RISM approach as a useful complement to numerical simulation for a reasoned analysis of aggregation properties in colloidal mixtures.

Received 5th August 2021,  
Accepted 26th September 2021

DOI: 10.1039/d1cp03604a

rsc.li/pccp

## 1 Introduction

At the mesoscale, complex fluids can be characterized as systems capable of self-assembly, *i.e.* to spontaneously form organized structures out of simpler building blocks. The comprehensive study of these patterns, along with the possibility to control their shape and size by tuning the interaction law, is among the greatest challenges of soft matter physics.

Recent studies have shown that a rich variety of mesoscopic patterns are obtained for asymmetrically-shaped particles whose constituent blocks interact through spherically-symmetric potentials.<sup>1–4</sup> In this regard, a versatile model is represented by Janus dimers, *i.e.* heteronuclear dimers in which one monomer is solvophilic and the other one is solvophobic.<sup>5,6</sup> The interest in this specific class of colloidal particles stems from their capability to be synthesized in a large variety of sizes, aspect ratios, and interaction properties,<sup>7–11</sup>

and from their high technological impact.<sup>12–14</sup> Moreover, Janus dimers are able to self-organize into various kinds of supracolloidal structures, provided that appropriate thermodynamic conditions are met,<sup>15–17</sup> as also observed in theoretical and simulation studies.<sup>18–20</sup>

Recently, we have undertaken an extended investigation of the phase behavior of a dilute colloidal mixture of Janus dimers and spherical particles, by means of computer simulation.<sup>21–24</sup> In our scheme, a dimer is modeled as a pair of tangent hard spheres of different size, while the other species is represented by a hard sphere. Beside the steric repulsion, the two species interact *via* a square-well attraction between small monomers and spheres. We take the square-well width to be small compared to the size of spheres, as is usual for colloidal systems, but at the same time large enough to allow for the formation of aggregates of dimers and spheres at low temperature.<sup>24</sup> Moreover, the absence of any dimer–dimer or sphere–sphere attraction reflects the implicit assumption that this kind of interaction is significantly weaker than the dimer–sphere attraction. Finally, the significant size asymmetry between the monomers constituting the dimers favors the encapsulation of

Dipartimento di Scienze Matematiche e Informatiche, Scienze Fisiche e Scienze della Terra, Università degli Studi di Messina, Viale F. Stagno d'Alcontres 31, 98166 Messina, Italy. E-mail: gmunao@unime.it

spheres.<sup>22</sup> Indeed, we have seen that, for sufficiently low densities and temperatures, spheres gather together *via* an effective mutual attraction mediated by small monomers, whereas the uncontrolled growth of aggregates – followed by coarsening into a macroscopic droplet – is prevented by the hindrance exerted by large monomers, which form a protective coating around the hard-sphere aggregates. As a result, liquid-vapor separation is preempted by the formation of supramolecular aggregates. We have documented a rich phase scenario arising for our mixture, in terms of diameter and concentration of spheres:<sup>24</sup> when the two species have similar sizes and the concentration is small, we observe the onset of small clusters of spheres covered by a layer of dimers; for larger concentrations, we find other self-assembled structures (*i.e.* gel-like networks and bilayers); finally, when spheres are substantially larger than dimers, we observe the formation of membranes (*i.e.* curved sheets) and occasionally vesicles. A wide variety of aggregates also exists in two dimensions, both on a plane<sup>25</sup> and on a spherical surface.<sup>26</sup>

Recently, a colloidal mixture with characteristics similar to ours has been synthesized and investigated experimentally.<sup>27</sup> At variance with the simulated mixture, real spheres tend to coalesce, whereas the inclusion of Janus dimers stabilizes them against aggregation, with an encapsulation mechanism in gratifying accordance with our simulation results.

In this paper we study the fluid phase behavior of the mixture, at fixed total density (higher than in previous studies) and as a function of the sphere concentration. Upon lowering the temperature from high values, local inhomogeneities first appear, thereafter followed by the formation of aggregates. Owing to the large number of parameters involved and due to long relaxation times, a systematic analysis of the fluid sector would greatly benefit from the availability of a theoretical scheme complementing the much more costly simulation approach. More generally, having reliable theoretical tools to perform a quick analysis of the structure and thermodynamics of a complex fluid with many parameters is of uppermost importance.

With this in mind, we assess the performance of the Reference Interaction Site Model (RISM) theory of molecular fluids,<sup>28</sup> which is benchmarked against the numerical data generated by Monte Carlo. The RISM formalism is one of the most effective tools to investigate the structure and thermodynamics of molecular fluids. Derived as a molecular generalization of the Ornstein-Zernike theory of simple fluids,<sup>29</sup> the RISM approach was originally intended for rigid molecules made up of hard spheres.<sup>30</sup> Later on, the theory was extended to more general systems by the inclusion of long-range forces and attractive interactions. With these improvements, the RISM theory was successfully applied to associating fluids like water<sup>31,32</sup> and other polar solvents.<sup>33,34</sup> Recently, RISM has been employed to investigate the statistical properties of colloids,<sup>35–37</sup> polymers,<sup>38</sup> macromolecules,<sup>39</sup> and nanoparticles.<sup>40</sup> We have used the RISM theory to study pure fluids of dimers, finding a reasonable agreement with simulation results and other theoretical approaches.<sup>41,42</sup>

As argued before, the origin of inhomogeneities in the sphere subsystem can be traced back to a competition between a (dimer-mediated) short-range attraction and a longer-range (again effective) repulsion. The same mechanism is actually at work in one-component fluids of SALR (Short-range Attractive and Long-range Repulsive) particles. While in SALR fluids the competing interactions are directly encoded in the shape of the isotropic pair potential, in our system the interplay between attraction and repulsion arises from the interaction between the species. SALR fluids are currently employed to mimic the behavior of a variety of soft materials<sup>43–49</sup> and, as such, they are largely investigated in the current literature; four recent reviews witness the broad interest in this topic.<sup>50–53</sup> In view of the intrinsic similarity of our mixture with a SALR fluid, we will analyze the former system by the same tools applied for the latter. In particular, since the onset of aggregation in a SALR fluid is generally manifested in the appearance of a low-wavevector peak in the static structure factor,<sup>54–57</sup> we expect a similar signature to occur in the various (partial and total) structure factors of the mixture. Among them, we will analyze those which convey the most sensitive information about the microscopic state of the mixture. The interpretation of structural data in terms of the characteristics of microscopic arrangement is another well established step in the study of SALR fluids. Here, we follow a similar approach for the mixture, by relying on the cluster analysis of Monte Carlo configurations as a means to map out the mesoscale structures. In this regard, we devise a simple and robust criterion to determine the maximum distance for which two spheres can be considered as bonded together, *i.e.* belonging to the same aggregate. This parameter is crucial in the attempt to uncover the nature of aggregates developing in the fluid.

The outline of the paper is the following. After describing the model and methods in Section 2, we present and discuss our results in Section 3. Concluding remarks and perspectives for future studies are reported in Section 4.

## 2 Model and methods

In our system, a dimer is modeled as a pair of tangent hard spheres with different diameters,  $\sigma_1$  and  $\sigma_2$ , in a fixed ratio  $\sigma_2 = 3\sigma_1$ . Spherical particles are represented as hard spheres of diameter  $\sigma_3 = \sigma_2$ , see Fig. 1. All interactions are hard-sphere-like with additive diameters  $\sigma_{ij} = (\sigma_i + \sigma_j)/2$ , except for the interaction between the small monomer and the sphere, which is given the form of a square-well attractive potential:

$$u_{13}(r) = \begin{cases} \infty & \text{if } r < \sigma_{13} \\ -\varepsilon & \text{if } \sigma_{13} \leq r < \sigma_{13} + \sigma_1 \\ 0 & \text{otherwise} \end{cases} \quad (1)$$

In the following,  $\sigma_2$  and  $\varepsilon$  are taken as units of length and energy, respectively, which in turn leads to a reduced number density  $\rho^* = \rho\sigma_2^3$  and a reduced temperature  $T^* = k_B T/\varepsilon$ ,  $k_B$  being Boltzmann's constant. Finally, we denote  $N_d$  and  $N_s$  the number of dimers and spheres, respectively. Hence,  $N = N_d + N_s$  is the total number of particles,  $\chi_d = N_d/N$  and  $\chi_s = 1 - \chi_d$  are the

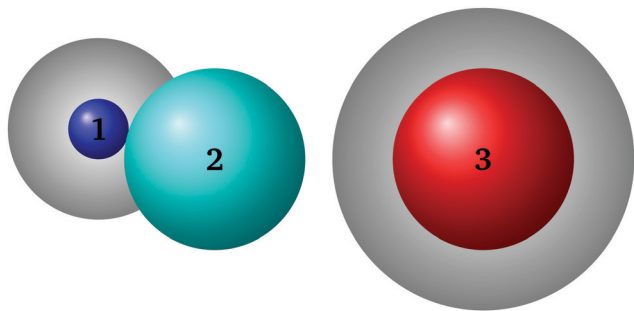


Fig. 1 The species making up our mixture: A dimer consists of a small (1, blue) and a large monomer (2, cyan) in a size ratio of  $\sigma_1/\sigma_2 = 1/3$ ; the spherical particle (3, red) has diameter  $\sigma_3 = \sigma_2$ . The grey halos around particles 1 and 3 represent the attractive region, extending up to  $\sigma_1$  beyond the distance of closest approach  $\sigma_{13}$ , see eqn (1).

relative concentrations of the two species, and we set  $\chi_{ds} = \sqrt{\chi_d \chi_s}$ .

To explore the behavior of the model in the fluid phase we employ the RISM approach: given an arbitrary molecular species, represented as a geometric assembly of  $n$  distinct interaction sites (like in a ball-and-stick model), the RISM theory provides a relationship between the set of  $n(n+1)/2$  site-site total correlation functions  $h_{ij}(r) = g_{ij}(r) - 1$  – with  $g_{ij}(r)$  being the radial distribution functions relative to sites  $i$  and  $j$  of different molecules – and the set of direct correlation functions,  $c_{ij}(r)$ . In reciprocal (wavevector) space, the RISM equation reads:<sup>29</sup>

$$\mathbf{H}(k) = \mathbf{W}(k)\mathbf{C}(k)\mathbf{W}(k) + \rho\mathbf{W}(k)\mathbf{C}(k)\mathbf{H}(k), \quad (2)$$

where  $\mathbf{H} \equiv [h_{ij}(k)]$  and  $\mathbf{C} \equiv [c_{ij}(k)]$  are  $n \times n$  symmetric matrices and  $\rho$  is the number density. The RISM formalism can be derived as a generalization of the Ornstein–Zernike relation for a mixture of monatomic species, where a matrix of intramolecular correlations  $\mathbf{W} \equiv [w_{ij}(k)]$  is introduced to account for the bonds between the interaction sites of a molecule. In particular,

$$w_{ij}(k) = \frac{\sin(kL_{ij})}{kL_{ij}}, \quad (3)$$

where  $L_{ij}$  is the bond distance between sites  $i$  and  $j$  of the same molecule. The RISM eqn (2) must be complemented by a “closure” relation, to form a closed set of equations; we have adopted to this scope the hypernetted-chain (HNC) approximation,<sup>29</sup>

$$c_{ij}(r) = \exp[-\beta u_{ij}(r) + \gamma_{ij}(r)] - \gamma_{ij}(r) - 1, \quad (4)$$

where  $\gamma_{ij}(r) = h_{ij}(r) - c_{ij}(r)$  and  $\beta = 1/T^*$ . HNC shows good performances when applied to the study of colloids<sup>41</sup> and cluster-forming liquids:<sup>58</sup> nevertheless, in the course of our study we have assessed its accuracy in comparison with other common closures, such as the Percus–Yevick and the Mean-Spherical Approximation.<sup>29</sup> In this way, we have ascertained the clear superiority of HNC for the mixture at issue, especially in the presence of aggregation, where the other schemes tend to drastically overlook the progressive structuring of the fluid.

Eqn (2) can be generalized to mixtures of molecular species and then specialized to the dimer–sphere system under study. In our case, all the matrices entering the formalism are  $3 \times 3$  matrices, and the intramolecular correlation matrix is explicitly given by

$$\mathbf{W}(k) = \begin{bmatrix} 1 & \frac{\sin(k\sigma_{12})}{k\sigma_{12}} & 0 \\ \frac{\sin(k\sigma_{12})}{k\sigma_{12}} & 1 & 0 \\ 0 & 0 & 1 \end{bmatrix} \quad (5)$$

Finally, the density  $\rho$  in eqn (2) is replaced by a diagonal matrix  $D$  with elements  $D_{11} = D_{22} = \rho\chi_d$  and  $D_{33} = \rho\chi_s$ .

We solve the set of coupled RISM/HNC equations numerically by means of an iterative Picard algorithm, using a real-space grid of  $2^{14}$  points and a mesh step of  $\Delta r = 0.001\sigma_2$ .

We shall present most of our structural results in terms of  $k$ -space correlations, *i.e.* in terms of the various structure factors characterizing the mixture. The dimer–dimer structure factor  $S_{dd}(k)$  reads:

$$\begin{aligned} S_{dd}(k) &= \frac{1}{2^2} \sum_{i,j=1,2} w_{ij}(k) + \frac{\rho\chi_d}{2^2} \sum_{i,j=1,2} h_{ij}(k) \\ &\equiv F(k) + S'_{dd}(k). \end{aligned} \quad (6)$$

The first term on the r.h.s. of (6) is the molecular form factor  $F(k)$ , which characterizes the shape of the dimer. The form factor accounts for the interference of radiation scattered from different parts of the same particle in a diffraction experiment. The correlations between different dimers are instead expressed by  $S'_{dd}(k)$ , which depends on the Fourier transform of the total correlation functions relative to monomers only. The sphere–sphere structure factor is

$$S_{ss}(k) \equiv S_{33}(k) = 1 + \rho\chi_s h_{33}(k), \quad (7)$$

and the dimer–sphere structure factor, involving the Fourier transform of the cross-correlation functions  $h_{13}(r)$  and  $h_{23}(r)$ , is given by

$$S_{ds}(k) = \frac{1}{2} \rho\chi_{ds} [h_{13}(k) + h_{23}(k)]. \quad (8)$$

In terms of the partial structure factors  $S_{dd}(k)$ ,  $S_{ss}(k)$ , and  $S_{ds}(k)$ , we can also define “total” structure factors, describing correlations between fluctuations of global variables, like for instance the total number density:

$$S_{NN}(k) = \chi_d S_{dd}(k) + 2\chi_{ds} S_{ds}(k) + \chi_s S_{ss}(k), \quad (9)$$

which is hereafter referred to as the total structure factor (see ref. 59 for details).

Moving to thermodynamic quantities, the isothermal compressibility  $K_T$  is given as a combination of  $k \rightarrow 0$  limits of the partial structure factors:<sup>29,60</sup>

$$\rho k_B T K_T = \frac{S_{dd}(0)S_{ss}(0) - [S_{ds}(0)]^2}{\chi_s S_{dd}(0) + \chi_d S_{ss}(0) - 2\chi_{ds} S_{ds}(0)}. \quad (10)$$

Finally, for a generic interaction-site model the internal energy reads

$$\frac{U}{N} = 2\pi\rho \sum_{i,j} \chi_i \chi_j \int_0^\infty u_{ij}(r) g_{ij}(r) r^2 dr, \quad (11)$$

where the sum runs over all interaction sites. For the present mixture, this formula is simply reduced to

$$\frac{U}{N\varepsilon} = -4\pi\rho\chi_d\chi_s \int_{\sigma_{13}}^{\sigma_{13}+\sigma_1} g_{13}(r)r^2 dr. \quad (12)$$

In the present work, RISM predictions are assessed against canonical-ensemble Monte Carlo (MC) simulations of a sample of  $N = 1372$  particles enclosed in a cubic box with periodic boundary conditions. A larger sample of 4000 particles is occasionally considered to estimate the size dependence of our results. As a general protocol, we have employed a million MC cycles to equilibrate the system, followed by twice longer production runs. In our scheme, a MC cycle involves  $N$  trial single-particle moves; for a dimer, either a trial displacement or a trial re-orientation is randomly attempted. The orientational move is implemented by the Barker and Watts procedure,<sup>61,62</sup> consisting in a trial rotation around a randomly chosen coordinate axis. The maximum extent of a displacement and the maximum rotation angle are adjusted during the equilibration stage in such a way as to ensure an acceptance ratio between 40% and 60%.

With specific concern to the hard-sphere subsystem, we have computed several properties to characterize the presence of local inhomogeneities and aggregates. In order to identify connected assemblies of hard spheres, we have used the Hoshen-Kopelman algorithm,<sup>63</sup> readily generalized to work with an off-lattice system of particles. A thorough discussion of the optimal choice of the “bond distance” between two hard spheres is deferred to the next Section. The cluster-size distribution,  $N(s)$ , is defined as in ref. 57 and 64:

$$N(s) = \frac{s}{N_s} \langle n(s) \rangle, \quad (13)$$

where  $\langle n(s) \rangle$  is the average number of clusters with size  $s$  per single configuration; the normalization of  $N(s)$  is such that

$\sum_s N(s) = 1$ . The cluster analysis is typically carried out on a set of 1000 configurations taken from the last part of the production run. We also monitor the total number of clusters, the fraction of isolated particles, the size of the largest aggregate, and the number of bonds per particle.

### 3 Results

We start discussing the accuracy of RISM calculations for the equimolar mixture, *i.e.*  $\chi_s = \chi_d = 0.5$ , using MC simulation data as a reference. Under equimolarity conditions, a quick survey indicates that RISM works best for densities in the range 0.20–0.30, while the theoretical predictions become less accurate for lower densities (for  $\rho^* \lesssim 0.1$ ). Hence, from now on we will focus our analysis on the thermodynamic states with total density  $\rho^* = 0.30$ .

In order to establish a useful benchmark, we consider a mixture of dimers and spheres at infinite temperature, where the square-well attraction is ineffective and only steric repulsions survive. Under these conditions, the fluid behaves as a homogeneous mixture of non-interacting hard dimers and hard spheres. Total correlations between spheres only [ $h_{33}(k)$ ] and large monomers only [ $h_{22}(k)$ ] are shown in Fig. 2A, as computed by RISM and MC. Perhaps not surprisingly, the two functions are practically coincident, even for  $\chi_s = 1$  (pure spheres) and  $\chi_s = 0$  (pure dimers), due to the negligible contribution of small monomers to the packing fraction of the mixture. Overall, RISM predictions agree reasonably well with MC data, except for a slight overestimate of the correlations at small wavevectors; it is clear that these discrepancies are due to the inescapable approximations of the theory, as well as to the known difficulty to get accurate results in this regime from simulation.

The profile of the total structure factor  $S_{\text{NN}}(k)$  is shown in Fig. 2B. All the terms entering eqn (9) are also reported in the

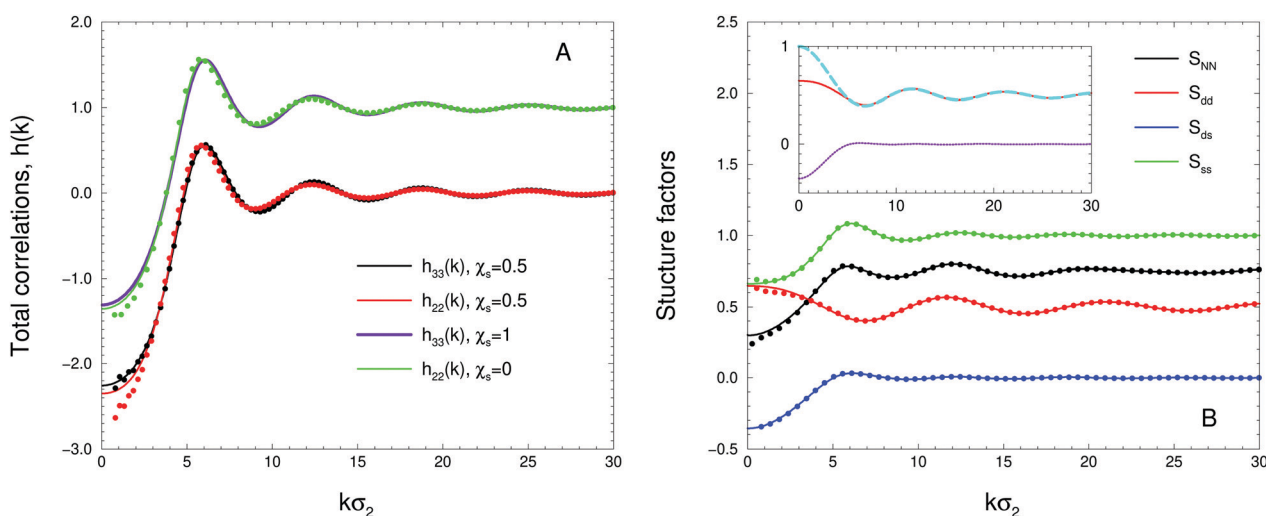


**Fig. 2** Mixture of dimers and spheres at infinite temperature and  $\rho^* = 0.30$ . (A) RISM predictions (lines) and MC data (symbols) for  $h_{33}(k)$  and  $h_{22}(k)$  ( $\chi_s$  values are given in the legend); for clarity, the curves for pure fluids are vertically shifted by one. (B) RISM (lines) and MC (symbols) for the various structure factors defined in eqn (6)–(9), for  $\chi_s = 0.5$ . In the inset,  $S_{\text{dd}}(k)$  (full red line) is resolved into intramolecular [ $F(k)$ , dashed cyan line] and intermolecular [ $S'_{\text{dd}}(k)$ , dotted indigo line] contributions, see eqn (6).

figure. It appears that the large  $k$  oscillations in  $S_{\text{NN}}(k)$  are mainly determined by the dimer–dimer contribution, which in turn reflects the properties of the form factor  $F(k)$ , as documented in the inset. Looking at the definitions, the various structure factors tend to different limits for large  $k$ :  $S_{\text{dd}}(k)$  has the same limiting value of  $F(k)$  [1/2 in our case, *i.e.* the inverse number of molecular sites, see eqn (6)];  $S_{\text{ss}}(k) \rightarrow 1$ , see eqn (7);  $S_{\text{ds}}(k) \rightarrow 0$ , see eqn (8); therefore,  $S_{\text{NN}}(k) \rightarrow \chi_{\text{d}}/2 + \chi_{\text{s}} = 0.75$  for an equimolar mixture, see eqn (9). We can appreciate the substantial agreement between RISM and MC, at least in the considered conditions, thus confirming the very good performance of the theory, which, we recall, was originally designed to describe correlations in purely steric fluids.

As the temperature is lowered, the square-well attraction becomes increasingly relevant and, in parallel, also the tendency of hard spheres to aggregate becomes more and more pronounced. In particular, a clear signature of aggregation is, as in SALR fluids, the onset of a low- $k$  peak in  $S_{\text{ss}}(k)$ , *i.e.* a peak preceding the main diffraction peak, see Fig. 3; here, RISM predictions (in panel A) are contrasted with MC results (panel B), with a more stringent comparison between the two in the inset. We see that the low- $k$  peak falls at  $k_0 \lesssim 2$ , *i.e.* well below the main diffraction peak at  $\approx 2\pi/\sigma_{33}$ . Looking first at the RISM results, the onset of local inhomogeneities is signaled by the development of an inflection point in the low- $k$  region for temperatures around  $T^* = 1.00$ , which then transforms into a shoulder for  $T^* = 0.50$ , before finally evolving into a well-shaped peak for  $T^* = 0.35$ . As the temperature is further lowered, the peak grows in height until reaching a maximum of  $\approx 0.95$  for  $T^* = 0.30$ . If we now try to reduce the temperature further, we run into a drawback, since the RISM algorithm fails to converge to a physically meaningful solution (typically, large oscillations show up in real-space correlations even for large distances or deep negative peaks appear in the structure factors). This outcome is not unexpected since RISM – like any other theory

designed for homogeneous fluids – only works for sufficiently high temperatures, where the spatial inhomogeneities are not too marked (or where the fluid does not enter too much within a liquid–vapor phase separation). Clearly, this problem does not affect simulation, and the subsequent MC evolution of the sphere–sphere structure factor below  $T^* = 0.30$  is reported in Fig. 3B. The small downward shift in the position of the low- $k$  peak on cooling, which is observed both in the RISM and in MC data, signals a corresponding reorganization of aggregates over larger and larger distances. The distribution of dimers in space follows the same trend of spheres: in particular, a low- $k$  peak emerges on cooling also in the functions  $h_{13}(k)$  and  $h_{23}(k)$  (not shown). This similarity of behavior is a clear manifestation of the crucial role of small monomers in providing the bridging “glue” between spheres, hence the structure factors of both species have the same gross features. The comparison between theory and simulation, reported in the inset of Fig. 3B, shows that RISM closely follows the MC evolution of  $S_{\text{ss}}(k)$ , even at the lowest temperature attainable by theory. Only the height of the low- $k$  peak is slightly underestimated, which again reflects the increasing difficulties encountered by RISM in keeping up with the enhancing of inhomogeneities on cooling.

The way how incipient aggregation is reflected in the various contributions making up the total structure factor  $S_{\text{NN}}(k)$  is shown in Fig. 4, referring to RISM calculations for  $T^* = 0.30$ . Here, a low- $k$  peak is present not only in  $S_{\text{ss}}(k)$ , but also in the structure factors involving dimers, *i.e.*  $S_{\text{dd}}(k)$  and  $S_{\text{ds}}(k)$ . As a result,  $S_{\text{NN}}(k)$  exhibits a local maximum at  $k \approx 1.5$ ; the latter position is an average determined from the superposition of various peaks located between 1 and 2. More generally, the profile of  $S_{\text{NN}}(k)$  faithfully follows that of the cross contribution  $S_{\text{ds}}(k)$  over the whole  $k$  range. This should be contrasted with the previous observation that, for purely steric interactions,  $S_{\text{NN}}(k)$  closely reflects  $S_{\text{dd}}(k)$ . For temperatures lower than  $T^* = 0.30$ , *i.e.* out of the reach of RISM, MC results (reported in the inset of Fig. 4) show that the low- $k$  peak grows on cooling.

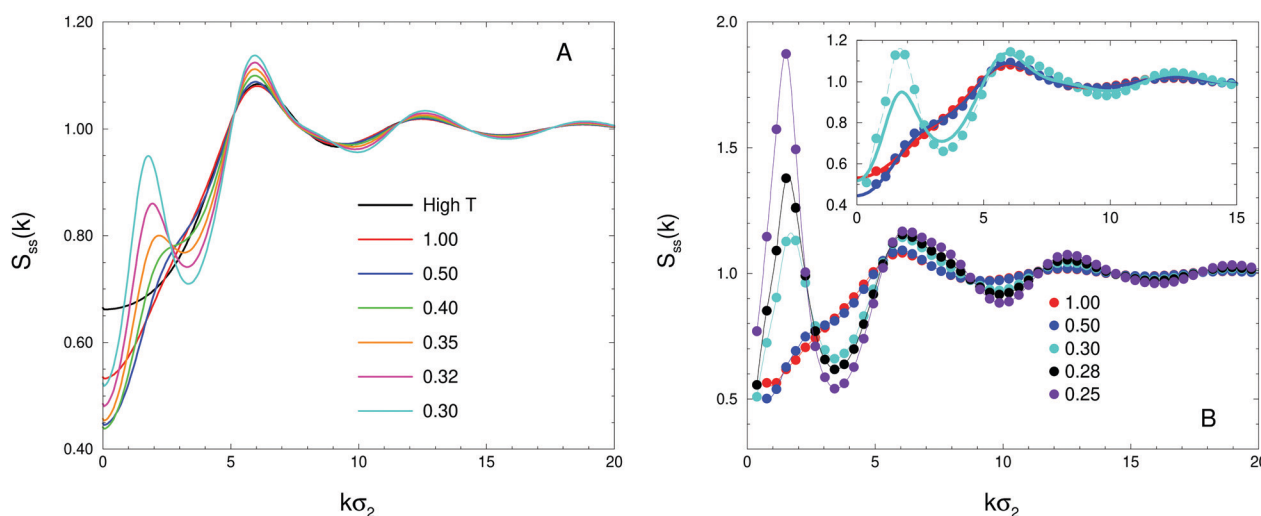


Fig. 3 Sphere–sphere structure factor  $S_{\text{ss}}(k)$  at equimolarity and progressively lower temperatures (see the legends). RISM (A) and MC (B, symbols, with lines as guides to the eye) are shown. Inset: Comparison between RISM predictions (thick lines) and MC data (symbols, with dashed lines as guides to the eye).

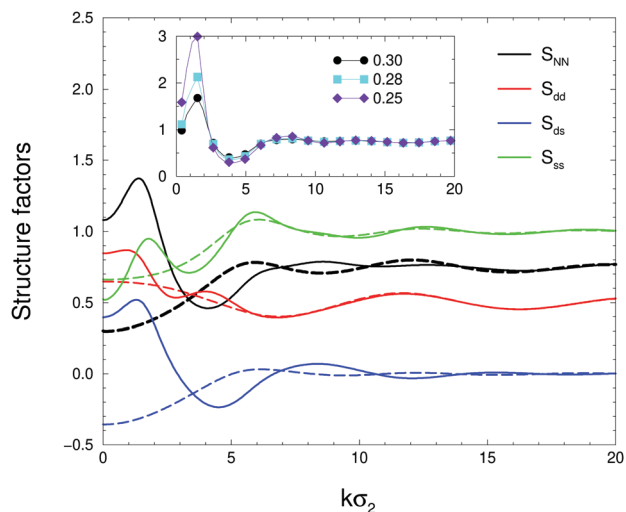


Fig. 4 RISM  $S_{NN}(k)$  resolved into various contributions, for  $T^* = 0.30$  and  $\chi_s = 0.5$  (full lines); for comparison, we also report the predictions for  $T = \infty$  (dashed lines), *i.e.* the same curves shown in Fig. 2B. Inset: MC  $S_{NN}(k)$  for low temperatures (in the legend).

Concerning thermodynamic properties, the compressibility of the fluid as computed by RISM is plotted in Fig. 5A as a function of the temperature. Looking for an assessment of this quantity by MC, we might think that an accurate check of RISM data cannot be carried out, due to the well known problem to extrapolate the  $k \rightarrow 0$  behavior of structure factors from finite-size simulations. In an attempt to remedy this difficulty, rather than extrapolating the individual MC structure factors down to  $k = 0$ , we have computed the r.h.s. of eqn (10) over the whole  $k$  range, see the inset of Fig. 5A. Here we note that RISM and MC substantially agree near  $k = 0$ , implying that the compressibility estimate provided by RISM can be deemed as good. From the same inset we see that the only  $k$  region where RISM deviates from MC is again near the low- $k$  peak. Turning back to the main panel, we observe that the compressibility moderately increases as the temperature is lowered at fixed concentration and density, with no hints at a diverging trend near the ultimate threshold of convergence of the RISM algorithm; hence, we can exclude any propensity of the mixture towards a macroscopic phase separation. This conclusion is clearly consistent with the presence of a low- $k$  peak in  $S_{NN}(k)$ , possibly evolving – at lower temperatures – to a divergence at finite  $k$ , like in other fluids with local inhomogeneities.

The internal energy per particle is shown in Fig. 5B. We see from this picture that, within its operating range, the RISM theory closely follows MC results. This good agreement reflects the accurate theoretical prediction of  $g_{13}(r)$ , as exemplified in the inset of panel B for two different temperatures. In the main panel, we see a progressive decrease of the internal energy on cooling, with the parabolic trend for  $T^* = 0.30$  replaced by a roughly linear behavior below this threshold.

Simulation offers the possibility to relate the emerging structural and thermodynamic features with the local arrangement of particles in the fluid. This opportunity prompts us to

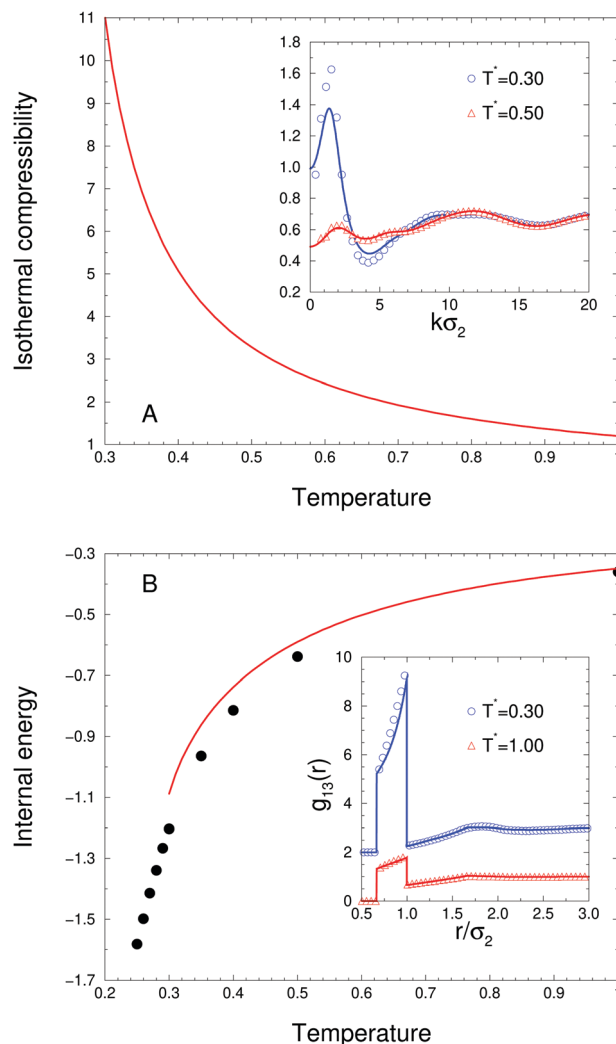


Fig. 5 (A) RISM isothermal compressibility at equimolarity as a function of temperature. Inset: The r.h.s. of (10) according to RISM (lines) and MC (symbols), extended over the whole  $k$  range for two different temperatures (see the legend). (B) RISM (lines) and MC (symbols) energies, for the same thermodynamic conditions as before. Inset:  $g_{13}(r)$  according to RISM and MC for two different temperatures (see the legend); for the sake of clarity,  $g_{13}(r)$  for  $T^* = 0.30$  has been vertically shifted by two.

carry out an extended analysis of aggregation properties, based on the microscopic configurations generated by MC. In order to characterize the aggregation properties of the mixture, a crucial issue is the definition of the “bond distance”  $d_{\text{bond}}$ , *i.e.* the distance within which two particles can be considered as bonded together. As a preliminary consideration, since spheres are non-interacting beyond the hard core, it is not straightforward to associate  $d_{\text{bond}}$  with the range of attractive interactions, as is commonly assumed in studies of SALR fluids. In our previous analysis,<sup>24</sup> two spheres were considered as bonded together when their distance was smaller than  $\sigma_3 + 3\sigma_1 \equiv 2\sigma_2$ , which represents – according to eqn (1) – the maximum distance at which two spheres can experience a mutual attraction mediated by a small monomer placed in the middle. However, this choice would lead to a too large value of the

bonding distance, given the relatively high density of our sample. Indeed, we have checked that  $d_{\text{bond}} = 2$  returns the unphysical outcome that all spheres belong to a single aggregate spanning the whole simulation box, even in the high temperature regime where attractive interactions are altogether absent. The same conclusion follows if we adopt another common choice, which is to set  $d_{\text{bond}}$  equal to the position of the first minimum in  $g_{33}(r)$  ( $\approx 1.8$ ). At the opposite end, if we were to use a too much restrictive criterion, for instance  $d_{\text{bond}} = 1.1$ , then we would conclude that aggregation is practically absent even at very low temperature, at variance with the picture emerging from the structural analysis.

Seeking an optimal bond distance in the interval between 1.1 and 1.8, we turn back to our high-temperature sample. We have computed a few aggregation properties as a function of  $d_{\text{bond}}$ , based on the available microscopic MC configurations. As reasonably expected, see Fig. 6 (left panel), the average fraction of isolated hard spheres per single configuration constantly decreases as  $d_{\text{bond}}$  grows, whereas the opposite occurs for the size of the largest cluster (middle panel). On the other hand, in the right panel we see that the total number of aggregates in the sample, whatever their size, shows a non-monotonic trend as a function of  $d_{\text{bond}}$ , with a maximum around 1.25. This outcome can be explained by observing that the number of aggregates initially grows with  $d_{\text{bond}}$ , since more and more spheres are allowed to join to each other at the expenses of isolated particles. However, beyond a certain threshold aggregates coalesce to form larger clusters and this progressively lowers their number. At this point, it is reasonable to take  $d_{\text{bond}} \approx 1.25$ , namely to assume as bond distance the value maximizing, at high temperature, the pool of possible outcomes in terms of number of aggregates. By this choice, we ensure that the counting of aggregates is the least sensitive to

small variations of  $d_{\text{bond}}$  from the point of maximum. Slightly anticipating the discussion of Fig. 9, the cluster-size distribution associated with  $d_{\text{bond}} = 1.25$  is characterized at high temperature by a sharp decay with size, with practically zero probability to find more than 10–12 particles connected together. In other words, even in the absence of attraction, small aggregates statistically form and dissolve following the natural MC evolution of the mixture. It is clear that, according to the proposed criterion,  $d_{\text{bond}}$  needs to be calculated every time the density of hard spheres is changed, for example when we change the relative concentration at fixed total density.

Choosing  $d_{\text{bond}} = 1.25$ , we have studied the same three properties in Fig. 6 as a function of temperature, in order to detect, from a microscopic viewpoint, the tendency of the system to form aggregates. This analysis is reported in Fig. 7. We see that the number of isolated spheres (left panel) drops upon cooling, until, for  $T^* = 0.25$ , only  $\approx 10\%$  of the spheres are non-bonded. At the same time, small aggregates progressively coalesce into larger units; as a result, the total number of clusters (right panel) rapidly decreases, while the size of the largest cluster (middle panel) increases, until it contains about 10% of all spheres in the mixture.

As the temperature is lowered, spheres reorganize themselves in space in such a way that their local environment becomes progressively denser. This can be seen from Fig. 8, where the number of bonds per sphere,  $N_{\text{bonds}}$ , is reported as a function of temperature. We see that the fraction of spheres engaged in one or more bonds steadily increases at the expenses of isolated ones. In particular, for  $T^* = 0.25$  more than 50% of the spheres are bonded to at least another sphere. Interestingly enough, for  $T^* = 0.30$  we see the first occurrence of a sphere with seven neighbors; spheres involved in eight bonds first show up for  $T^* = 0.28$ .

A more detailed picture of the microscopic arrangement of hard spheres is provided by the cluster-size distribution [eqn (13)], reported in Fig. 9 for  $\chi_s = 0.5$ . We note that  $N(s)$  undergoes a sharp decay for  $T^* = 0.35$ . In the range

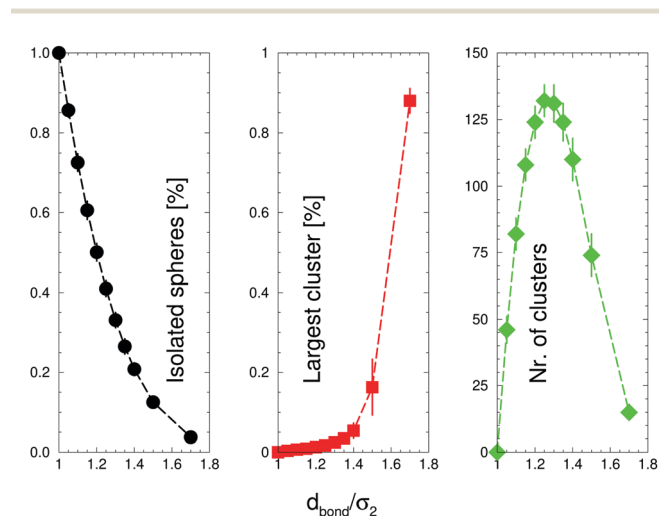


Fig. 6 MC data for the fraction of isolated spheres (left), the largest cluster size (center), and the total number of clusters (right), as a function of  $d_{\text{bond}}$  for  $\chi_s = 0.5$  and infinite temperature. Average values per single configuration, as computed over about 1000 configurations uniformly distributed along the last part of the MC trajectory, are reported with the corresponding statistical uncertainties. Lines are guides to the eye.

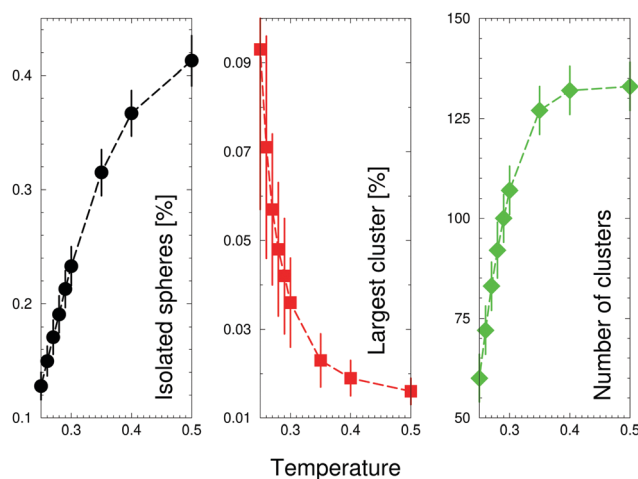


Fig. 7 Same properties as in the previous figure, but for fixed  $d_{\text{bond}} = 1.25\sigma_2$ , plotted as functions of temperature for  $\chi_s = 0.5$ .

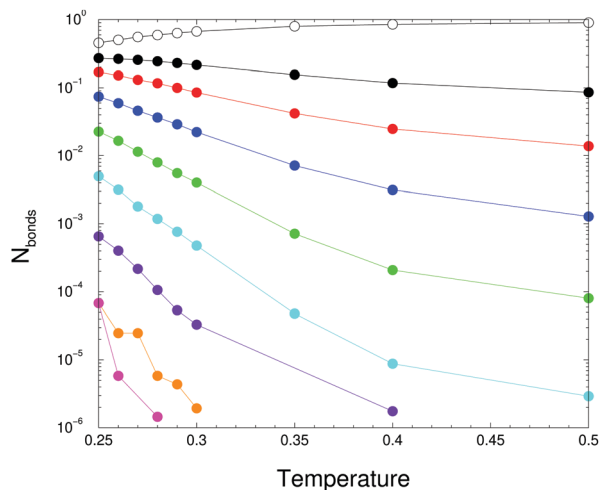


Fig. 8 Number of bonds per sphere plotted as a function of temperature for  $\chi_s = 0.5$ . From top to bottom,  $N_{\text{bonds}} = 0, 1, \dots, 8$ .

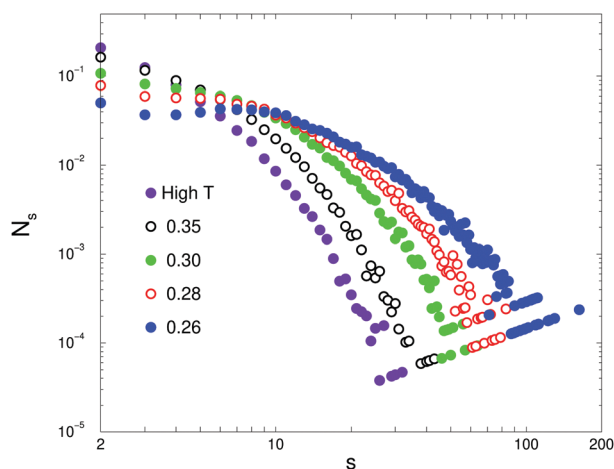


Fig. 9 Cluster-size distribution of hard spheres for a few selected temperatures (see the legend) and for  $\chi_s = 0.5$ .

$T^* = 0.30$ – $0.27$  the decay is less sharp and an inflection point occurs, until eventually, for  $T^* = 0.26$ , we find for the first time the occurrence of a local peak in the distribution, signaling the presence of clusters (or, better, “aggregates”) preferentially composed by  $\approx 10$  spheres (over a pool of 686 hard spheres), whereas the largest aggregate involves about 70 spheres (see also the middle panel of Fig. 7); only occasionally aggregates with more than 100 spheres are seen.

At this point, we can gather together all structural (Fig. 3 and 4) and microscopic information (Fig. 9), to attempt a unified picture of the phase behavior of the fluid mixture upon cooling. Again, our reasoning is inspired by similar studies of one-component SALR fluids.<sup>56,57</sup> At very high temperature, no low- $k$  peak is found in the structure factors; in this case the fluid is fully homogeneous and the cluster-size distribution is characterized by a sharp decay of the probability associated with the formation of clusters of increasing size – always

allowed by random fluctuations, even in the absence of any attraction. As the temperature is lowered, a low- $k$  peak first appears and then steadily grows in height ( $T^* = 1.00$ – $0.27$ ); correspondingly, the fluid displays local inhomogeneities that are progressively more marked;  $N(s)$  is still characterized by a monotonic decay and the fluid is said to exhibit “intermediate-range order”;<sup>56,57</sup> as soon as a maximum appears in  $N(s)$  (here for  $T^* = 0.26$ ), a more definite “clustered state” is entered, with the location of the maximum signaling the typical size of clusters.

The analysis presented so far already demonstrates the appearance of aggregates in the system at low temperature. However, it gives no information about their structure. Even though a geometric characterization of the aggregates is out of the scope of the present paper, some information can be got from a visual inspection of microscopic configurations. To exemplify, we show the top panel of in Fig. 10 a typical snapshot of the equilibrated sample for  $T^* = 0.25$ . To avoid the breaking of aggregates at the boundary of the box, we have first computed the center of mass of each aggregate, according to the procedure devised by Bai and Breen;<sup>65</sup> then, for each particle in a given aggregate we have considered its closest replica to the center of mass. We see that a large aggregate generally takes an elongated, relatively open conformation, with no appreciable branching. This evidence can be explained by looking at the

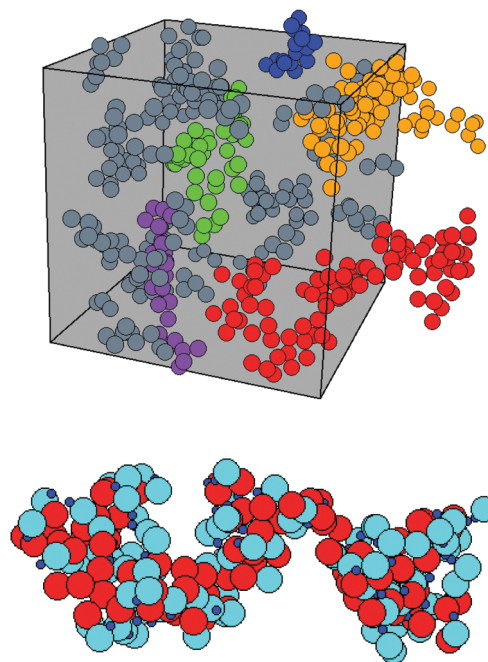


Fig. 10 Top: Microscopic picture of an equilibrium configuration for  $T^* = 0.25$  and  $\chi_s = 0.5$ . For a better visualization, neither dimers nor isolated spheres ( $\approx 80$ ) are shown. Most aggregates are formed by less than 10 spheres (in grey). The largest cluster (in red) is formed by  $\approx 90$  spheres, followed in descending order by aggregates with 75 (orange), 42 (green), 26 (purple), and 17 (blue) spheres. Bottom: Detail of the largest aggregate, with spheres (red) drawn together with their neighboring dimers; according to the color convention of Fig. 1, large monomers are colored in cyan, small ones in blue.



detailed structure of the largest aggregate, shown in the bottom panel of Fig. 10, where each sphere is plotted together with its neighboring dimers, which are those for which the 1–3 distance falls within the attraction range of eqn (1). As is clear, spheres are joined together by small monomers placed in the interstitial spaces between them; large monomers form a layer around spheres, with a double effect; on one hand, this inert coating prevents the possibility for spheres to come closer to each other, thus preventing aggregates to assume a more compact, globular form that is associated with the common concept of “cluster” of particles. Secondly, the same hindrance effect prevents aggregates from coalescing together, so to form a single or few large droplets which would typically herald a full phase separation. We do not follow the ultimate fate of our fluid at still lower temperatures, where it eventually becomes structurally arrested.<sup>24</sup>

Having broadly characterized the properties of the mixture under equimolar conditions, the last part of our study is devoted to the analysis of other values of the sphere concentration  $\chi_s$ , while still holding the overall density fixed at  $\rho^* = 0.30$ . In this regard, we observe that changes in the concentration of spheres do not appreciably affect the overall convergence properties of the RISM algorithm; in particular, the lowest temperature that can be attained by RISM is still  $T^* = 0.30$ . RISM predictions will be discussed near this low-temperature threshold only.

Starting from thermodynamics, MC and RISM energies per particle are shown in Fig. 11 for various concentration values. Both schemes substantially agree in signaling that the strongest cohesion between spheres and dimers is attained when the former are slightly less numerous than the latter (*i.e.* for  $\chi_s \approx 0.3$ – $0.4$ ). More precisely, RISM predicts a minimum energy for  $\chi_s = 0.45$ , only slightly shifted from the MC datum  $\chi_s = 0.40$ . Overall, RISM agrees with MC all over the concentration range, though the RISM minimum is more rounded and slightly overestimated.

In order to link the energy information with the microscopic arrangement of particles, we have preliminarily determined the value of  $d_{\text{bond}}$  for a number of concentration values, by repeating the same calculation previously described for  $\chi_s = 0.5$  (where  $d_{\text{bond}} = 1.25$ ). Results are shown in Fig. 12A. When the number of spheres is large, *e.g.*, for  $\chi_s = 0.9$ , the bond distance

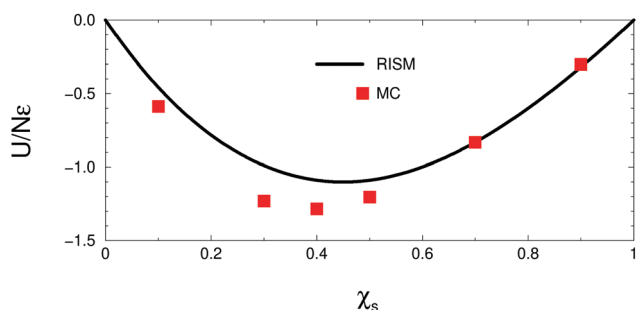


Fig. 11 RISM (lines) and MC (symbols) internal energies per particle, plotted as functions of the concentration for  $T^* = 0.30$  and  $\rho^* = 0.30$ .

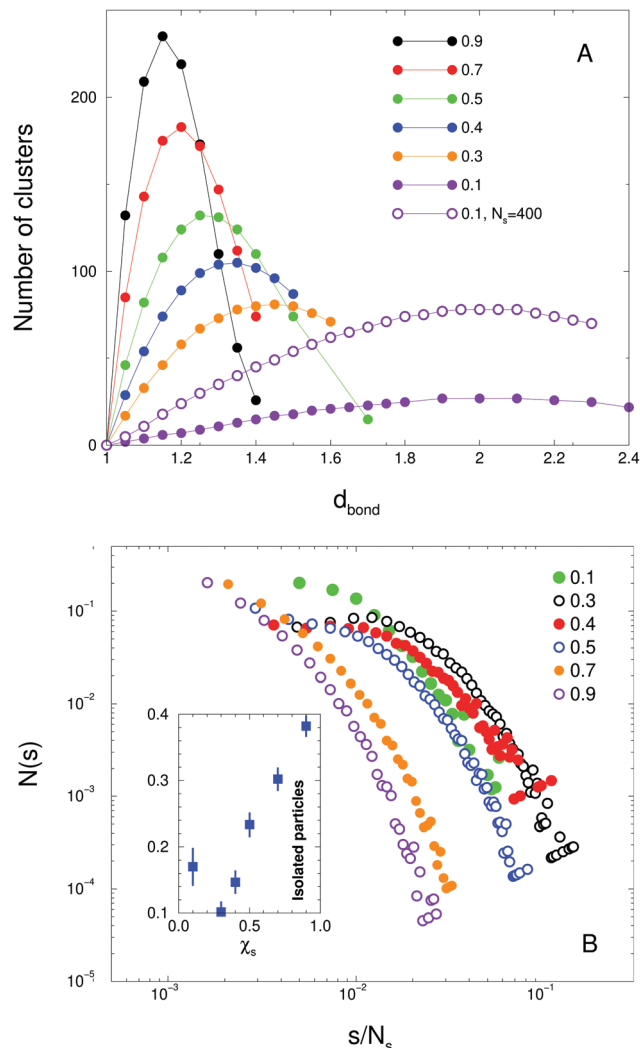


Fig. 12 (A) Total number of clusters plotted as a function of  $d_{\text{bond}}$  for decreasing concentration of spheres (see the legend) at infinite temperature. Open circles refer to a sample composed by a total of  $N = 4000$  particles. (B) Cluster-size distribution for a few  $\chi_s$  values (see the legend), for  $T^* = 0.30$ . For a better comparison, the cluster size  $s$  has been normalized by the number of spheres at the given concentration. Inset: Fraction of isolated particles vs.  $\chi_s$ .

is reduced to  $d_{\text{bond}} = 1.15$ , which is coherent with the general premises of our method: at higher densities, spheres are closer together; hence a maximum in the number of aggregates falls at shorter  $d_{\text{bond}}$ . As the concentration of spheres decreases,  $d_{\text{bond}}$  increases until it attains the upper limit of  $d_{\text{bond}} = 2$  for  $\chi_s = 0.1$ . In this limit, the contact distance becomes equal to the interaction distance. Simulations with 4000 particles for  $\chi_s = 0.1$  (open circles in Fig. 12A) show that, despite a systematic increase in the number of clusters, the general shape of the curve and the location of the maximum are left unchanged.

Once the value of  $d_{\text{bond}}$  has been set for every  $\chi_s$ , we can compute the cluster-size distribution for  $T^* = 0.30$  (see Fig. 12B). For a better comparison between the various concentrations, the cluster size has been normalized to the number of spheres present in the mixture at the given  $\chi_s$ . The overall

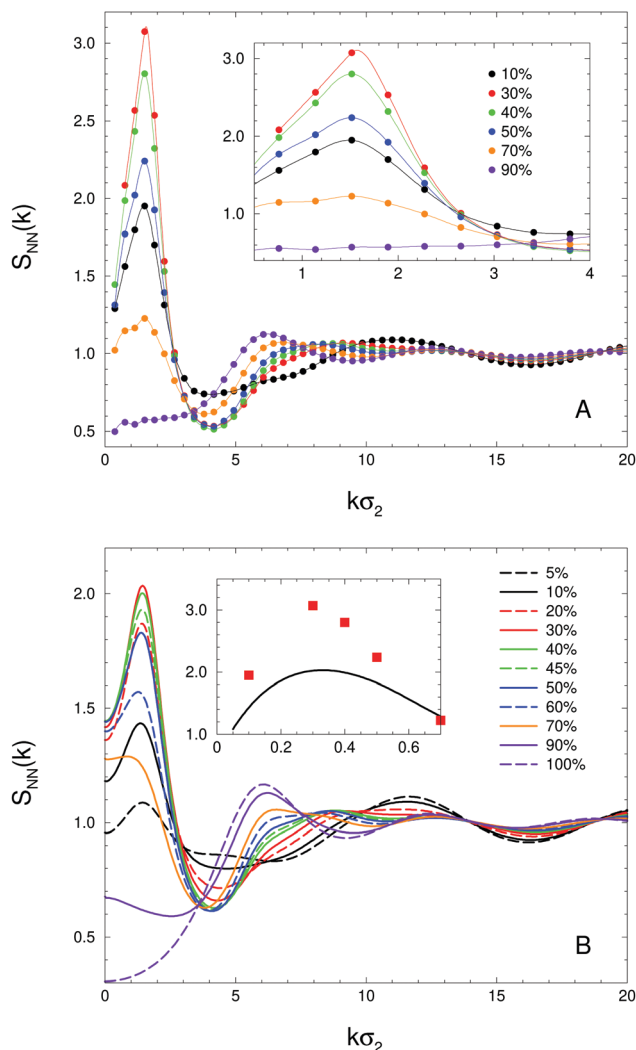


Fig. 13 (A) MC  $S_{NN}(k)$  for various  $\chi_s$  values (see the legends) and  $T^* = 0.30$ . Inset: Magnification of the low- $k$  peak. (B) Same property, as predicted by RISM. Inset: Height of the low- $k$  peak according to MC (squares) and RISM (line).

appearance of  $N(s)$  complies with the picture emerging from the behavior of internal energy: when spheres dominate (*e.g.*, for  $\chi_s = 0.9$ ), the few dimers present are insufficient to provide the “glue” necessary to join all the spheres together, thus leading to a sharp decay of  $N(s)$ , which is tantamount to a large fraction of isolated spheres ( $\approx 40\%$ , see the inset). Things change when dimers are progressively added. When  $\chi_s$  drops to 0.5, still 25–30% of the spheres remain isolated and  $N(s)$  is shifted towards larger  $s$ . At the opposite end ( $\chi_s = 0.1$ ), dimers are so many that the number of isolated spheres is reduced to  $\approx 17\%$ ; in this case,  $N(s)$  extends to larger  $s$  in comparison with  $\chi_s = 0.7$  or 0.9. In between, the largest number of contacts between spheres and dimers is obtained for  $\chi_s = 0.3$ –0.4, where only a few spheres (roughly 10% of the total) are not involved in the aggregation process and  $N(s)$  extends to the largest  $s$  values of all. All indications now agree to conclude that the optimal conditions for the stabilization of the mixture are met for

$\chi_s = 0.3$ –0.4. Looking at Fig. 12B, we see that  $N(s)$  shows a monotonic decay for  $\chi_s = 0.1$  and in the interval 0.5–0.9; as discussed before, under these conditions the fluid exhibits intermediate-range order. On the other hand,  $N(s)$  shows a plateau for  $\chi_s = 0.4$ , which for  $\chi_s = 0.3$  gives way to a shallow local maximum around  $s \approx 5$ , indicating the preferential development of aggregates with that size. In both cases, the mixture is closer in temperature to conditions favorable to the development of a clustered state, similarly as found for  $\chi_s = 0.5$  and  $T^* = 0.26$ .

Finally, the total structure factor  $S_{NN}(k)$  is reported in Fig. 13 for  $T^* = 0.30$ , where results from MC simulation (A) and RISM theory (B) are shown for various concentrations of spheres. As for MC, a low- $k$  peak is practically absent for  $\chi_s = 0.9$  and only hardly seen for  $\chi_s = 0.7$  (see also the inset); a more distinct peak is visible for  $\chi_s = 0.1$  and 0.5, whereas the low- $k$  peak reaches its maximum height for intermediate concentrations, *i.e.* for  $\chi_s = 0.3$ , and 0.4. Hence, a gratifying agreement is found between the shape of the low- $k$  peak and the information gathered from the previous cluster analysis. All this witnesses the good quality of the procedure followed in the definition of  $d_{\text{bond}}$ , since a coherent indication is returned from two independent (microscopic and structural) sources. We may appreciate in Fig. 13B how RISM theory faithfully reproduces the same trends emerging from MC; in particular, the low- $k$  peak is slightly higher for  $\chi_s = 0.3$  than for  $\chi_s = 0.4$ . As already discussed in the equimolar case, for the lowest temperatures RISM underestimates the structural correlations; this can be seen from the inset of panel B, where the height of the low- $k$  peak is plotted as a function of concentration.

## 4 Conclusions and perspectives

Using RISM theory and Monte Carlo (MC) simulations, we have carefully investigated early stages of aggregation in the fluid phase of a colloidal mixture of asymmetric dimers and spherical particles. All interactions in the model are hard-sphere-like, except for an additional square-well attraction between the small monomer and the sphere. Our study is carried out in a temperature regime where the fluid exhibits local inhomogeneities, which on cooling evolve into more structured aggregates. The origin of these spatial modulations can be rationalized in terms of the competition between a short-range (small monomer-sphere) attraction and a longer-range repulsion (due to the steric hindrance of large monomers). A clear structural indication of the emergence of spatial inhomogeneities is provided by the development of a low-wavevector peak in the structure factors of the mixture, as indeed signaled by both theory and simulation. In order to acquire microscopic evidence of the existence of aggregates, we have carried out a cluster analysis of a high number of representative microscopic configurations taken from simulation.

As a matter of fact, as the fluid mixture proceeds towards the full-fledged aggregated state, the RISM algorithm eventually fails to converge to a physically meaningful solution. Despite

being only appropriate for moderately inhomogeneous systems, the RISM theory agrees reasonably well with MC within its range of applicability, in that it provides reliable structural indications of the existence of inhomogeneities in the system, which become fully developed slightly outside the thermodynamic region where the theory is well-behaved.

With the indications acquired from theory, we plan to complement the information obtained from simulation so as to arrive at a thorough understanding of the mixture behavior as a function of density, temperature, and concentration. In particular, it would be interesting to connect the fluid phase properties with the low-temperature behavior in the high dilute regime, where we have documented a rich phase scenario with the formation of different supramolecular aggregates, whose specific nature depends on the size ratios and relative concentration of the species.<sup>24</sup>

A particularly relevant issue when employing a theory like RISM concerns the possibility to characterize the underlying microscopic arrangement of an aggregating fluid only in terms of structural indicators, namely without explicitly resorting to microscopic data from simulations. Much effort toward this interpretation has been devoted in the field of pure SALR fluids, and currently three different heuristic structural criteria have been proposed: in short, the first one is based on the height of the low- $k$  peak in the static structure factor, as the fluid progresses within the clustered state;<sup>56,57</sup> the second criterion is based on the definition of a cluster-cluster correlation length, to be deduced by a Lorentzian fit of the same low- $k$  peak;<sup>66,67</sup> the third criterion, involving real-space properties, is based on the development of a long-distance shell of neighbors in the radial distribution function of the fluid.<sup>58,68,69</sup> It would be highly desirable to verify the possibility to apply these criteria also for mixtures.

Finally, we have introduced a novel method – based on a microscopic analysis of the high-temperature regime, where attraction becomes ineffective – to compute the maximum distance within which two particles can be considered as bonded together. In forthcoming studies we plan to carefully assess the scope of this criterion within the realm of cluster-forming fluids. Should the validity of our approach not be limited to the case under study, this would be a noteworthy result since, as also observed in the context of SALR particles, an accurate choice of the bond distance is crucial to properly identify the self-assembled structures emerging at low temperature.

## Conflicts of interest

There are no conflicts to declare.

## References

- G. Avvisati and M. Dijkstra, *Soft Matter*, 2015, **11**, 8432.
- J. R. Wolters, G. Avvisati, F. Hagemans, T. Vissers, D. J. Kraft, M. Dijkstra and W. K. Kegel, *Soft Matter*, 2015, **11**, 1067.
- H. W. Hatch, J. Mittal and V. K. Shen, *J. Chem. Phys.*, 2015, **142**, 164901.
- H. W. Hatch, S.-Y. Yang, J. Mittal and V. K. Shen, *Soft Matter*, 2016, **12**, 4170.
- F. Tu, B. J. Park and D. Lee, *Langmuir*, 2013, **29**, 12679.
- B. J. Park and D. Lee, *ACS Nano*, 2012, **6**, 782.
- J.-W. Kim, R. J. Larsen and D. A. Weitz, *J. Am. Chem. Soc.*, 2006, **128**, 14374.
- D. Nagao, C. M. van Kats, K. Hayasaka, M. Sugimoto, M. Konno, A. Imhof and A. van Blaaderen, *Langmuir*, 2010, **26**, 5208.
- S. Chakraborty, J. A. Yang, Y. M. Tan, N. Mishra and Y. Chan, *Angew. Chem.*, 2010, **49**, 2888.
- T. S. Skelton, Y. Chen and S. A. F. Bon, *Langmuir*, 2014, **30**, 13525.
- K. Yoon, D. Lee, J. W. Kim, J. Kim and D. A. Weitz, *Chem. Commun.*, 2012, **48**, 9056.
- J. D. Forster, J. G. Park, M. Mittal, H. Noh, C. F. Schreck, C. S. O'Hern, H. Cao, E. M. Furst and E. R. Dufresne, *ACS Nano*, 2011, **5**, 6695.
- I. D. Hosein and C. M. Liddell, *Langmuir*, 2007, **23**, 10479.
- F. Ma, S. Wang and N. Wu, *Adv. Funct. Mater.*, 2012, **22**, 4334.
- D. J. Kraft, R. Ni, F. Smalenburg, M. Hermes, K. Yoon, D. Weitz, A. van Blaaderen, J. Groenewold, M. Dijkstra and W. Kegel, *Proc. Natl. Acad. Sci. U. S. A.*, 2012, **109**, 10787.
- T. S. Skelton, Y. Chen and S. A. F. Bon, *Soft Matter*, 2014, **10**, 7730.
- H. Hu, *et al.*, *ACS Nano*, 2016, **10**, 7323.
- G. Munaò, P. O'Toole, T. S. Hudson, D. Costa, C. Caccamo, A. Giacometti and F. Sciortino, *Soft Matter*, 2014, **10**, 5269.
- J. R. Bordin, L. B. Krott and M. C. Barbosa, *Langmuir*, 2015, **31**, 8577.
- G. Munaò, P. O. Toole, T. S. Hudson, D. Costa, C. Caccamo, F. Sciortino and A. Giacometti, *J. Phys.: Condens. Matter*, 2015, **37**, 234101.
- G. Munaò, D. Costa, S. Prestipino and C. Caccamo, *Phys. Chem. Chem. Phys.*, 2016, **18**, 24922.
- S. Prestipino, G. Munaò, D. Costa and C. Caccamo, *J. Chem. Phys.*, 2017, **146**, 084902.
- G. Munaò, D. Costa, S. Prestipino and C. Caccamo, *Colloids Surf., A*, 2017, **532**, 397–404.
- S. Prestipino, D. Gazzillo, G. Munaò and D. Costa, *J. Phys. Chem. B*, 2019, **123**, 9272–9280.
- S. Prestipino, G. Munaò, D. Costa, G. Pellicane and C. Caccamo, *J. Chem. Phys.*, 2017, **147**, 144902.
- N. Dlamini, S. Prestipino and G. Pellicane, *Entropy*, 2021, **23**, 715.
- J. R. Wolters, J. E. Verweij, G. Avvisati, M. Dijkstra and W. K. Kegel, *Langmuir*, 2017, **33**, 3270–3280.
- D. Chandler and H. C. Andersen, *J. Chem. Phys.*, 1972, **57**, 1930–1937.
- J. P. Hansen and I. R. McDonald, *Theory of simple liquids*, 3rd Edn, Academic Press, New York, 2006.
- L. J. Lowden and D. Chandler, *J. Chem. Phys.*, 1974, **61**, 5228–5241.

- 31 L. Lue and D. Blankschtein, *J. Chem. Phys.*, 1995, **102**, 5427–5437.
- 32 A. Kovalenko and F. Hirata, *Chem. Phys. Lett.*, 2001, **349**, 496.
- 33 B. M. Pettitt and P. J. Rossky, *J. Chem. Phys.*, 1983, **78**, 7296–7299.
- 34 D. Costa, G. Munaò, F. Saija and C. Caccamo, *J. Chem. Phys.*, 2007, **127**, 224501.
- 35 L. Harnau, J.-P. Hansen and D. Costa, *Europhys. Lett.*, 2001, **53**, 729.
- 36 D. Costa, J.-P. Hansen and L. Harnau, *Mol. Phys.*, 2005, **103**, 1917.
- 37 G. Munaò, D. Costa, F. Sciortino and C. Caccamo, *J. Chem. Phys.*, 2011, **134**, 194502.
- 38 J. P. Hansen and C. Pearson, *Mol. Phys.*, 2006, **104**, 3389.
- 39 P. G. Khalatur, L. V. Zherenkova and A. R. Khokhlov, *J. Phys. II France*, 1997, **7**, 543.
- 40 W. Kung, P. González-Mozuelos and M. O. de la Cruz, *Soft Matter*, 2010, **6**, 331.
- 41 G. Munaò, D. Costa, A. Giacometti, C. Caccamo and F. Sciortino, *Phys. Chem. Chem. Phys.*, 2013, **15**, 20590.
- 42 G. Munaò, F. Gámez, D. Costa, C. Caccamo, F. Sciortino and A. Giacometti, *J. Chem. Phys.*, 2015, **142**, 224904.
- 43 P. Baglioni, E. Fratini, B. Lonetti and S. H. Chen, *J. Phys.: Condens. Matter*, 2004, **16**, S5003–S5022.
- 44 A. I. Campbell, V. J. Anderson, J. S. van Duijneveldt and P. Bartlett, *Phys. Rev. Lett.*, 2005, **94**, 208301.
- 45 F. Cardinaux, A. Stradner, P. Schurtenberger, F. Sciortino and E. Zaccarelli, *Europhys. Lett.*, 2007, **77**, 48004.
- 46 A. Stradner, H. Sedgwick, F. Cardinaux, W. C. K. Poon, S. U. Egelhaaf and P. Schurtenberger, *Nature*, 2004, **432**, 492.
- 47 P. D. Godfrin, S. D. Hudson, K. Hong, L. Porcar, P. Falus, N. J. Wagner and Y. Liu, *Phys. Rev. Lett.*, 2015, **115**, 228302.
- 48 J. Riest and G. Nägele, *Soft Matter*, 2015, **11**, 9273–9280.
- 49 J. Riest, G. Nägele, Y. Liu, N. J. Wagner and P. D. Godfrin, *J. Chem. Phys.*, 2018, **148**, 065101.
- 50 Y. Zhuang and P. Charbonneau, *J. Phys. Chem. B*, 2016, **120**, 7775–7782.
- 51 M. B. Sweatman and L. Lue, *Adv. Theory Simul.*, 2019, **2**, 1900025.
- 52 Y. Liu and Y. Xi, *Curr. Opin. Colloid Interface Sci.*, 2019, **39**, 123–136.
- 53 J. L. Bretonnet, *AIMS Mater. Sci.*, 2019, **6**, 509.
- 54 Y. Liu, L. Porcar, J. Chen, W.-R. Chen, P. Falus, A. Faraone, E. Fratini, K. Hong and P. Baglioni, *J. Phys. Chem. B*, 2011, **115**, 7238.
- 55 P. Falus, L. Porcar, E. Fratini, A. F. W.-R. Chen, K. Hong, P. Baglioni and Y. Liu, *J. Phys.: Condens. Matter*, 2012, **24**, 064114.
- 56 P. D. Godfrin, R. Castañeda-Priego, Y. Liu and N. Wagner, *J. Chem. Phys.*, 2013, **139**, 154904.
- 57 P. D. Godfrin, N. E. Valadez-Perez, R. Castañeda-Priego, N. Wagner and Y. Liu, *Soft Matter*, 2014, **10**, 5061.
- 58 J.-M. Bomont, D. Costa and J.-L. Bretonnet, *Phys. Chem. Chem. Phys.*, 2020, **22**, 5355–5365.
- 59 N. H. March and M. P. Tosi, *Introduction to liquid state physics*, World Scientific Publishing, 2002.
- 60 N. W. Ashcroft and D. C. Langreth, *Phys. Rev.*, 1967, **159**, 500.
- 61 J. Barker and R. Watts, *Chem. Phys. Lett.*, 1969, **3**, 144–145.
- 62 M. P. Allen and D. J. Tildesley, *Computer Simulation of Liquids*, Clarendon Press, USA, 1989.
- 63 J. Hoshen and R. Kopelman, *Phys. Rev. B: Condens. Matter Mater. Phys.*, 1976, **14**, 3438–3445.
- 64 S. H. Chen, J. Rouch, F. Sciortino and P. Tartaglia, *J. Phys.: Condens. Matter*, 1994, **6**, 10855–10883.
- 65 L. Bai and D. Breen, *J. Graphics GPU Game Tools*, 2008, **13**, 53–60see also.
- 66 R. B. Jadrich, J. A. Bollinger, K. P. Johnston and T. M. Truskett, *Phys. Rev. E: Stat., Nonlinear, Soft Matter Phys.*, 2015, **91**, 042312.
- 67 J. A. Bollinger and T. M. Truskett, *J. Chem. Phys.*, 2016, **145**, 064902.
- 68 J.-M. Bomont, D. Costa and J.-L. Bretonnet, *Phys. Chem. Chem. Phys.*, 2017, **19**, 15247–15255.
- 69 J.-M. Bomont, D. Costa and J.-L. Bretonnet, *AIMS Mater. Sci.*, 2020, **7**, 170.